

# Imaging Spectrometry in High-Alpine Topography: The Derivation of Accurate Broadband Albedo

Stephan Gruber<sup>a</sup>, Daniel Schläpfer<sup>b</sup> and Martin Hoelzle<sup>a</sup>

<sup>a</sup> Glaciology and Geomorphodynamics Group, Department of Geography, University of Zurich, Winterthurerstr. 190, CH-8057 Zurich, Switzerland, email: stgruber@geo.unizh.ch

<sup>b</sup> Remote Sensing Laboratories, Department of Geography, University of Zurich, Winterthurerstr. 190, CH-8057 Zurich, Switzerland

## ABSTRACT

Three flight lines over high-alpine terrain have been recorded with the imaging spectrometer DAIS7915 in August 2002. The aim of this campaign was the derivation of broadband albedo to support distributed energy-balance modelling. The data was successfully ortho-rectified and a vicarious calibration as well as topographic-atmospheric correction were performed. To enable the derivation and investigation of black-sky and white-sky albedo, two-parameter kernel-based BRDF models were fitted to subsets. Coupling of these BRDF-models with the energy-balance code PERMEBAL suggests a significant influence of angular anisotropy on net radiation in complex topography. Comparison of modeled and measured time series of albedo show a good representation of its temporal evolution, but a large offset between the ground measurements and the BRDF model inversions is present.

**Keywords:** Albedo, BRDF, mountains, block surface, imaging spectrometry, energy-balance modeling

## 1 INTRODUCTION

Albedo is defined as the reflected fraction of incident radiation. It is therefore one of the most important factors that influence the ground surface energy-balance. For models of boundary layer processes and atmosphere-ground interactions it is one of the most sensitive surface characteristics to be measured or parameterized. This paper describes the derivation of broadband short-wave albedo from DAIS7915 hyperspectral imagery over complex alpine terrain together with corresponding sensitivity studies. As this work is aimed at the provision of data to a specific model, a short description of that model together with its purpose is provided.

PERMEBAL [1],[2] is a model of atmosphere-cryosphere interaction in high-mountain regions developed at the University of Zurich in recent years. Due to the enhanced magnitude of global climatic change in mountain systems [3],[4] and its expected influence on natural hazards [5] the development of corresponding models is presently receiving growing attention. PERMEBAL simulates daily vertical energy-balances for each cell of a two-dimensional grid, based on spatial data on surface characteristics and daily meteorological time series. The model typically operates on cell sizes of 10-50m. The build-up as well as the melting of the winter snow cover are successfully simulated [6]. During summer, snow-free conditions and high solar elevation result in strong energy input into the ground. Then, snow-free albedo (a spatially variable surface characteristic) greatly affects short-wave net radiation. It is therefore desirable to investigate and describe spatial data fields of summer albedo.

A verification campaign and sensitivity analyses with PERMEBAL show that the current level of absolute accuracy is better than  $\pm 1$  °C for mean annual surface temperatures in steep rock walls of different expositions. Modeled and measured daily time series at 14 locations are correlated to 60-90%. A deviation of  $\pm 1$  °C corresponds to an absolute error in albedo of  $\pm 0.05$ - $0.08$  (or 25-35% relative) for areas of medium insolation, assuming an otherwise perfect model. However, these errors contain both the effect of an estimated uniform albedo at each point and the errors inherent in the model algorithms. The absolute accuracy in the final albedo product therefore should be better than  $\pm 0.05$ .

The aim of this study is the derivation of a spatial data field of snow-free albedo and estimate its errors. The effect that the solar incidence-angle dependence of albedo has on net radiation in complex topography needs to be investigated at this level of accuracy. Furthermore, this campaign will provide first experience with preprocessing and correction of imaging spectrometer data in complex terrain.

## 2 BACKGROUND AND METHODS

The reflective behavior of most natural surfaces is variable both spectrally and angularly, i.e. as a function of illumination and measurement geometry. This surface behavior is mathematically described by the bidirectional reflectance distribution function (BRDF) [7] for each wavelength. Spectral albedo or bihemispherical reflectance (following the naming conventions put forward in [8]) in one waveband also depends on the angular distribution of incident radiation due to the angular anisotropy in most BRDFs. Broadband albedo is furthermore influenced by the spectral characteristic of incident light due to the spectral integration of narrowband albedos.

Several BRDF models have been developed to describe the behavior of the bidirectional reflectance in appropriate and simple mathematical terms. A review is provided by [9]. Using several measurements under varying illumination and viewing geometries, appropriate models may be selected and their parameters fitted. Subsequently, these models describe the reflectance for angles that have not been measured. In kernel-based models [10]-[12], the BRDF is expanded into a linear sum of terms (the so-called kernels), characterizing different scattering modes. The model parameters are the weights assigned to each kernel in the linear sum. The derivation of albedo from a kernel-based model characterizing the BRDF of a target is described in detail by [10]. The two extreme cases of completely diffuse and isotropic illumination (white-sky albedo) and completely direct illumination (black-sky albedo) are differentiated. Black-sky albedo is the directional-hemispherical integral of the BRDF model and therefore a function of the solar incidence angle. White-sky albedo is the bihemispherical integral of the BRDF model and a constant for a given wavelength. Natural illumination conditions are always intermediate values between these two cases, assuming the diffuse fraction of illumination to be isotropic. Finally, broadband albedo is derived by integration of spectral albedos over the desired waveband, weighted by the illuminating spectral solar flux.

For meteorological applications, albedo usually refers to the waveband between about 300 and 2500nm wavelength, covering most of the average solar irradiation at ground level. Other definitions ranging up to 3000 or 5000nm exist. Wavelengths shorter than 300nm are effectively absorbed by ozone. Beyond 2500nm, solar irradiance is minimal and largely absorbed by atmospheric water. Short-wave albedo is determined by dividing the measurements of two pyranometers, one for the downwelling and one for the upwelling radiative flux. Each measures over the solid angle  $2\pi$  (a full hemisphere). The glass domes over the sensors are usually opaque to radiation outside the 300-3000nm band.

## 3 FIELD SITE

The Corvatsch area is situated in the south-east of Switzerland, close to the town of St. Moritz at latitude:  $46^{\circ} 26'$  and longitude:  $9^{\circ} 50'$ . The area lies between 1800 and 3700m a.s.l. and is characterized by steep slopes, and high mountain features such as glaciers and extensive block fields in the periglacial zone. The area has been one of the prime sites for the investigation of permafrost and periglacial processes during the last 30 years [13] and research here benefits from a wealth of base data as well as easy access by cable car.

## 4 MEASUREMENTS

On 14 August 2002, three flight lines (Table 1) were recorded with the imaging spectrometer DAIS7915 [14] under perfectly cloudless sky. Areas above 3000m a.s.l. were snow-covered due to recent snow fall. A DGPS base station has been operated for the post-processing of the aircraft path. A Reagan Solar Radiometer was used to support characterization of the atmosphere and a GER 1500 spectro-radiometer was used to collect field spectra during the overpass.

**Table 1.** Details of DAIS7915 flight lines acquired on 14 August 2002 over Corvatsch, Switzerland.

	Time UTC	Image lines	Scan frequency	Flight elevation	Flight heading	Solar elevation	Solar azimuth	Clouds	Cast shadow
<b>Line 1</b>	10:05	1865	11.5Hz	6040m	$358^{\circ}$	$53.7^{\circ}$	$146.1^{\circ}$	none	0.8%
<b>Line 2</b>	09:52	2094	13.0Hz	6040m	$358^{\circ}$	$52.2^{\circ}$	$140.9^{\circ}$	none	1.4%
<b>Line 3</b>	10:20	2370	14.5Hz	6040m	$358^{\circ}$	$54.9^{\circ}$	$151.4^{\circ}$	none	0.6%

Two targets of 30\*30m were characterized by more than 200 measurements each using an ASD FieldSpec Pro Fr spectro-radiometer, several days before the overpass. Finding homogenous areas of that size is extremely difficult in the periglacial zone. An almost horizontal moraine surface and a scree slope with a slope angle of about

30° were selected. Both targets had virtually no vegetation cover and are expected not to have changed their reflective behavior between the field measurement and the data flight. For the moraine target this assumption has been verified with the GER1500 measurement during the overpass.

Since 1997, a meteorological station is recording up- and downwelling short-wave radiation on the rock glacier Murtèl using two Kipp & Zonen CM3 pyranometers. Their spectral range is 300-3000 nm and the accuracy for daily totals of either sensor is reported by the manufacturer to be  $\pm 10\%$ . The combined uncertainty in the albedo is believed to be better than  $\pm 10\%$  because the usual accuracy of these sensors is known to be better than the value stated by the manufacturer.

## 5 PREPROCESSING

### 5.1 Geometric Correction

The DAIS7915 imagery has been geometrically corrected using the software package PARGE [15]. Ground control points (GCP) were taken from digital maps and orthophotos. The digital elevation model with a final pixel size of 10m has been generated photogrammetrically. The PARGE quality control parameters listed in Table 2 indicate the successful achievement of pixel-accuracy. In complex topography this carries special significance as illumination and viewing geometries as well as surface characteristics are laterally extremely variable.

**Table 2.** Quality control parameters of PARGE processing indicate pixel-accuracy. INS: inertial navigation system.

	No of GCPs	Offset INS attitude		Offset DGPS flight path	
		RMS (roll)	RMS (pitch)	RMS (X)	RMS (Y)
<b>Line 1</b>	39	4.47 m	4.27 m	4.53 m	4.30 m
<b>Line 2</b>	25	4.54 m	4.70 m	4.63 m	4.41 m
<b>Line 3</b>	18	3.26 m	4.04 m	3.43 m	4.14 m

Almost each final pixel contained a real measurement due to the large across-track over-sampling of DAIS7915. The final image cube was generated by assigning nearest measurements to each pixel. This resulted in many imaging spectrometer measurements being lost, while preserving original, measured spectra.

### 5.2 Radiometric Quality

In order to verify the quality of the recorded imagery, a quality assessment based on visual inspection and image statistics was performed using the radiance values of the laboratory-calibrated image cube. In all three flight lines striping is visible for the bands 41-45 and 59-72, which are all part of spectrometer 3. In bands 1-19, about 5% of all pixels are saturated due to fresh snow exceeding the sensors dynamic range. Negative radiance values are caused by errors in the sensor or by inadequate calibration and are thus indicative of problematic channels. Most bands of the spectrometer 3 (SWIR-2) have between 10 and 45% negative pixels (Figure 2). The fluctuations in negative pixel abundance per band are small (2-7%) between flight lines, suggesting a rather stable cause of error. Only bands 52,53,55 and 56 always have less than 5% of negative values.

Noise can be estimated from homogeneous targets in the image cube and thus an order of magnitude for the signal to noise ratio (SNR) of each band can be established to support data quality control. A target of deep water was selected on lake Silvaplana assuming it to be spectrally flat at the ground instantaneous field of view (GIFOV) of around 10m. The noise was calculated as the standard deviation of the signal minus its 3x3 boxcar average for 25,000 pixels. Using a region of 165,000 pixels, the mean and standard deviation of the expected signal range for rock surfaces and alpine meadows has been determined, excluding very low values of water bodies and very high or saturated values for snow. The thus calculated SNR (Figure 1) represents a rather high estimate, as noise levels from water likely underestimate true noise levels in brighter targets. Nevertheless, a comparison of individual channels is facilitated.

Combining the above evidence, only the reflective channels 1-36, 38 and 39 are of satisfactory quality. However, for supporting the derivation of broadband albedo, the four best SWIR-2 channels 52, 53, 55 and 56 are used as well, adding up to a total of 42 used bands.

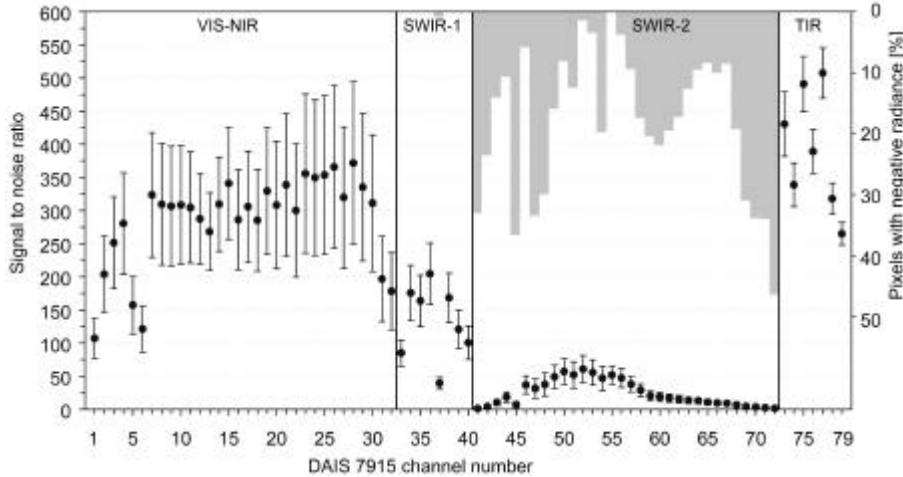


**Figure 1.** Image-based signal-to-noise ratio and the percentage of negative pixels (gray columns, right axis). The bad performance of the SWIR-2 spectrometer is evident.

### 5.3 Atmospheric and Topographic Correction, Vicarious Calibration

Atmospheric-topographic correction has been performed using the software package ATCOR4 [16]. A standard atmosphere with rural aerosol type and water vapor content of 10g/cm<sup>2</sup> (sea level to space) and 80km visibility have been employed. The resulting reflectance values are nadir-corrected hemispherical-directional reflectance factors (HDRF, cf. [8]), assuming Lambertian behavior.

Comparison of these HDRF spectra to ground spectro-radiometric measurements and library clear-water spectra revealed unacceptably large errors in the laboratory calibration of DAIS7915. A vicarious two-point calibration has been performed using the bright moraine and the deep clear water of lake Silvaplana as targets.

## 6 ALBEDO RETRIEVAL

### 6.1 Fitting of BRDF Kernels

For the fitting of kernel-based BRDF models, the solar incidence angle ( $\phi_0$ ), the view angle ( $\phi_s$ ) and the relative azimuth angle ( $\Psi'$ ) need to be known. In complex mountain topography, these vary considerably over short distances. The angles  $\theta_0$  and  $\theta_s$  are determined between the surface normal and the vectors to the sun and the sensor, respectively. The relative azimuth is the angle between the projection of the vectors to the sun/sensor onto the plane perpendicular to the surface normal. This relies on the assumption, that for our area of interest the angular properties of a tilted surface remain the same as for the horizontal case. For e.g. forest, this assumption would not be valid as trees grow vertically on a steep slope and not normal to it. BRDF model fits are calculated using the algorithms and code described by [9] based on AMBRALS (Algorithm for Modis Bidirectional Reflectance Anisotropy of the Land Surface) developed by [12] for the MODIS BRDF and albedo product [10].

Fitting of a BRDF model to each pixel or very few pixels is not feasible since only one or two observations are available for each pixel and the geometry will be affected by noise that is always present in digital elevation model derivatives in complex topography. Therefore, adequate subsets of the image are used for the derivation of a BRDF model. This model then represents the mean reflectance and the mean BRDF shape for the chosen subset. This model can be used for a) investigating the role of angular anisotropy in complex terrain and b) defining the BRDF model for every pixel of the subset using a multiplicative correction. This correction however relies on two hypotheses that need to be tested: 1) the BRDF model adequately characterises each pixel of the subset and 2) the shape of the BRDF does not change significantly within the chosen subset.

For lines 1 and 2, masks for a) alpine meadows; b) vegetation-free blocks and moraines and c) the rock glacier Murtèl were derived. The small Murtèl mask was generated manually, while the others were based on a spectral angle mapper classification. Several kernels and kernel combinations were tested on the data (spectral HDRFs and the angles  $\phi_0$ ,  $\phi_s$  and  $\Psi'$  for each pixel) sampled within these masks. The three-parameter model comprising an isotropic, a volume-scattering, and a geometrically-scattering kernel generally performed badly resulting in mostly negative weights for the geometric kernel. A two-parameter model was chosen. In almost all cases, the combination

between isotropic and RossThick [11],[12] kernels performed best. Especially on block fields it is surprising to see the volume scattering kernel outperform the geometric one.

Each model fit results in two coefficients per band together with a value for  $R^2$  for the fit per band. The  $R^2$  value contains both the error in the model fit in terms of its shape as well as the error due to brightness variations within the class.

## 6.2 Derivation of Spectral Albedo from BRDF Kernel Models

Following the approach described by [10], spectral black-sky and white-sky albedos can be obtained using the pre-computed directional-hemispherical and bihemispherical kernel integrals, the derived model coefficients and the solar incidence angle.

## 6.3 Narrowband to Broadband Conversion

The derivation of broadband albedo involves the weighted integration of narrowband albedos. The weights for each band are proportional to the irradiant energy in the waveband represented by that measurement. The weights as well as the result of this integration are therefore a function of the spectral characteristics of the illumination. The method used for interpolation between measured bands and extrapolation outside the measured wavelengths influences the result significantly. Especially the extrapolation assumptions for blue and UV light are very sensitive and can affect the broadband albedo in the range of  $\pm 5-10\%$ . In our approach, the extrapolation into the UV range is achieved by a multiplying the spectral albedo of the shortest wavelength by 0.8.

The irradiance spectra shown in Figure 2 were simulated using MODTRAN 4.0 [17]. As black-sky and white-sky albedo mark two extreme cases of illumination conditions, the weights for their integration from spectral albedos are also determined separately, assuming that with increasing diffuse radiation also the spectral characteristics change. The weights for direct illumination are determined from a clear-sky spectrum with a solar zenith angle of  $30^\circ$  and the weights for diffuse illumination from a spectrum assuming a position surrounded by a stratus cloud.

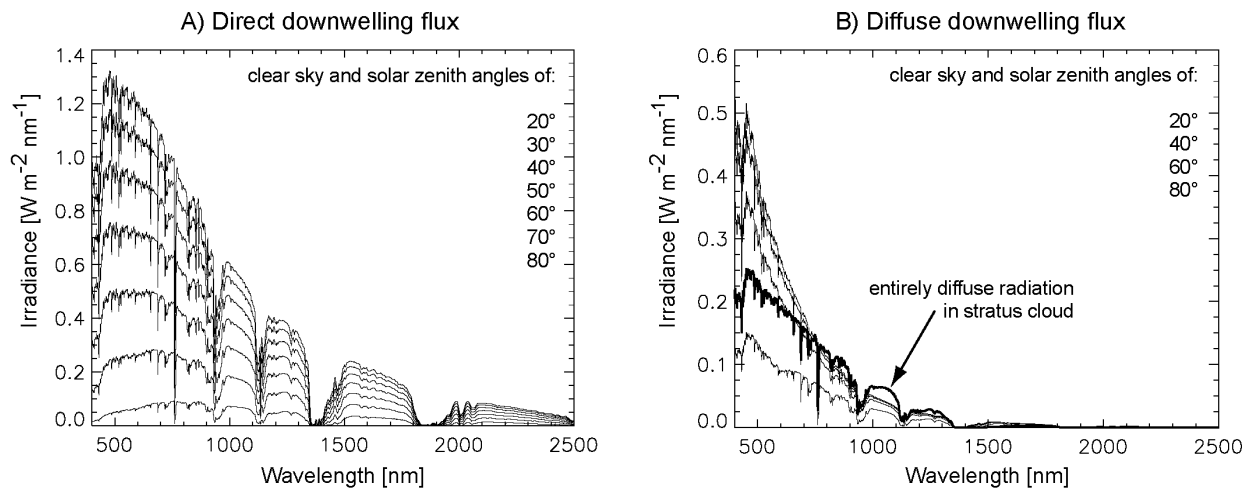


**Figure 2.** Spectra of the downwelling short-wave flux. A) direct radiation; B) diffuse radiation.

## 7 SENSITIVITY ANALYSIS FOR BRDF-MODEL DERIVED ALBEDO IN STEEP TOPOGRAPHY

Now that mean BRDF models have been derived based on subsets, these models can be used to investigate the influence of angular anisotropy on net radiation in steep terrain. The question is: how big is the difference in effective albedo between a northern slope (generally large solar incidence angles, large proportion of diffuse illumination) and a southern slope, given exactly the same surface characteristics? The magnitude of this difference in relation to the targeted accuracy determines whether a constant value for albedo suffices or albedo needs to be parameterised by an angular model.

Based on hourly standard meteorological data on global radiation from the station Corvatsch made by the Swiss Meteorological Service, the radiation regime for different slopes was parameterised for 1999 using the algorithms

implemented in PERMEBAL. The algorithm proposed by [18] and verified in the test area by [2] is used to parameterise the ratio of direct and diffuse radiation. Calculating the solar illumination geometry and sky-view factors as described in [2], hourly total short-wave insolation is parameterised for slopes of 0°, 10°, 20°, 30°, 40° and 50°, north-facing and south-facing. The calculated parameters are: solar incidence angle (in relation to surface normal), diffuse radiation and direct radiation. Table 3 summarizes the model results.

**Table 3.** Mean annual percentage of direct short-wave downwelling radiation (% direct) and annual mean of daily short-wave downwelling radiation totals (sw-down [W/m<sup>2</sup>]) for the modeled slopes.

slope	50° N	40° N	30° N	20° N	10° N	0°	10° S	20° S	30° S	40° S	50° S
% direct	42.9	43.1	43.3	42.5	44.1	47.2	49.4	50.9	53.1	53.7	53.5
sw down	160.6	162	163.6	165.5	169	170.8	186.5	198.6	206.6	210.4	209.4

Black-sky albedo was calculated for every hour and slope angle based on the BRDF models for the rock glacier Murtèl as well as alpine meadows and the modeled solar incidence angle. The percentage of direct and diffuse radiation determines the weights for black and white-sky albedo in the calculation of hourly net radiation. The so derived one-year time series were compared by defining the mean annual BRDF-derived albedo as: the total annual short-wave upwelling radiation over the total annual short-wave downwelling radiation. This is a radiation-weighted averaging of albedo which also reflects the net effect on the surface energy balance. Figure 3 illustrates the deviation of this effective mean annual BRDF-derived albedo from the white-sky albedo that is a possible constant substitute for it (solid lines). Dashed lines are calculated only from 15 July to 15 September, assuming a snow cover during winter. In order to demonstrate that the observed anisotropy does not originate from different weights used for the diffuse and direct spectral integration, one model run was performed with equal spectral integration weights for diffuse and direct radiation (blocks, equal weights).

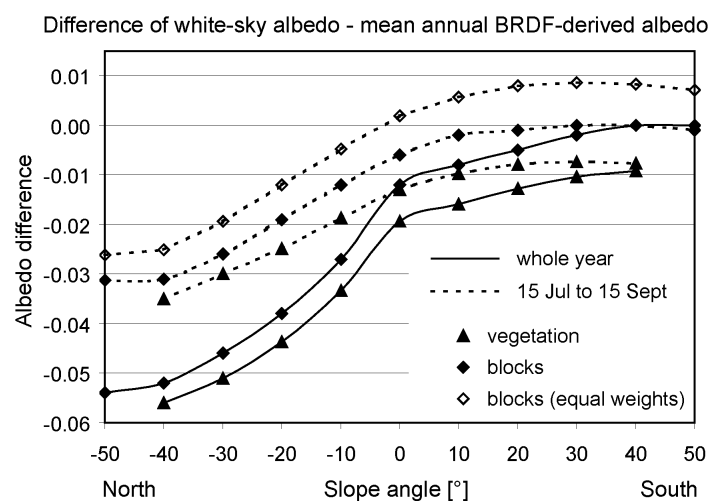


**Figure 3.** Difference of white-sky albedo and mean annual BRDF-derived albedo for different slope angles. Negative angles indicate northern slopes, positive angles southern slopes. See text for further details.

This illustrates, that an absolute error of up to -0.05 (25% relative error) in albedo has to be taken into account when neglecting its angular anisotropy. This indicates, that BRDF effects may significantly influence the ground - surface radiation balance.

## 8 IMAGE CORRECTION

The derivation of albedo for each image pixel (or for subsets) requires a correction procedure that applies the BRDF model inversion to each measurement; cf. [9] for detailed treatment of this problem. The basic assumption is the adequate representation of the real angular behaviour of each image (global or subset) pixel by the kernel-based model. Two applications are investigated here: 1) multiplicative BRDF-normalization 2) scaling of black- and white-sky albedo to measured image HDRF values.

The multiplicative correction factor is obtained by dividing the kernel-model result for the chosen geometry (desired  $\varphi_0$ ,  $\varphi_S=0$  and  $\Psi'=0$ ) by the model result for the geometry of the imaging spectrometer measurement. The multiplication of the measured HDRF with this factor will perform a BRDF-normalization of the image. The corrected image shows the expected nadir HDRF for every pixel if the image was recorded in flat topography.

After the derivation of black- and white-sky albedo from the BRDF model, these need to be scaled to the observed HDRF values if albedo per pixel is desired without sufficient angular measurements in one pixel. The underlying assumption is a linear scaling of the BRDF-model integrals. The correction factor is determined by division of the measured HDRF by the value predicted by the kernel-model. Black and white-sky albedo can be scaled using this factor.

## 9 VALIDATION

### 9.1 Comparison of flight lines 1 and 2

Figure 4 provides a visual impression of the pre-processed imagery as well as of the results of the BRDF-normalization and the albedo retrieval. Band 20 of lines 1 and 2 was combined into a checkerboard mosaic.

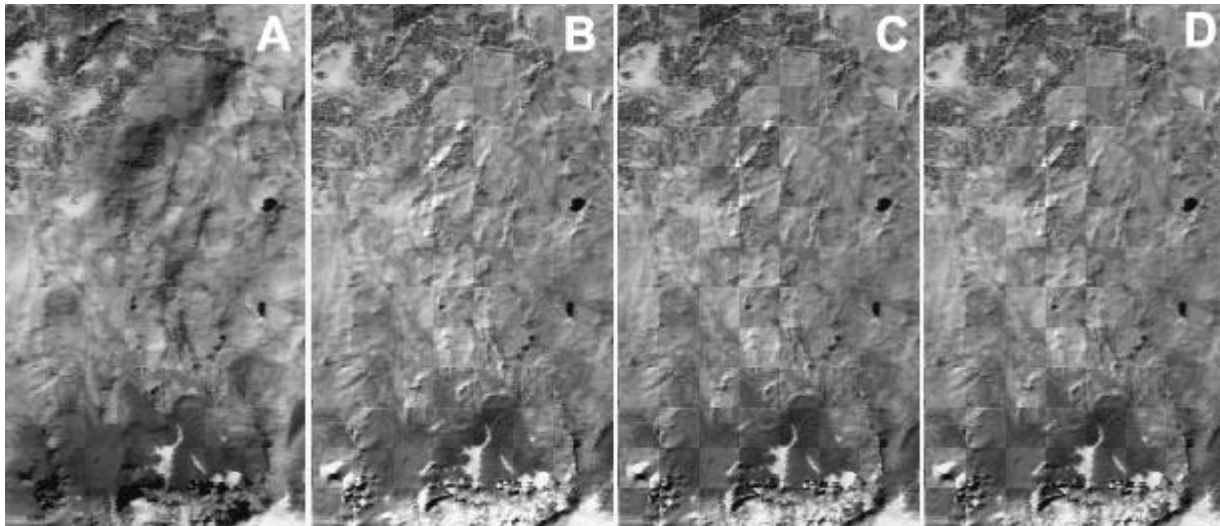


**Figure 4.** Visual comparison of lines 1 and 2 in a checkerboard mosaic of band 20. A) geometrically corrected data; B) result of topographic-atmospheric correction using ATCOR4; C) BRDF-normalized image and D) white-sky albedo

The successful correction of dark low-illumination areas during topographic-atmospheric processing as well as a reduction of the bright BRDF-effects by the BRDF-normalization are discernible in Figure 4. However, it is also visible that the checkerboard pattern becomes more prominent with increasing processing level and the extraction of higher-value data products. This visualizes the degree of misrepresentation of reality in the models used. Ideally, the images should become more alike during processing which is aimed at retrieving surface characteristics. Table 4 provides a preliminary comparison between lines 1 and 2 at different processing stages.

**Table 4.** Comparison of lines 1 and 2 at different processing levels and for subsets of blocky surfaces and alpine meadows. B-norm: BRDF-normalized, albedo: white-sky albedo

Subset	Coefficient of correlation between images				Relative difference between image means		
	geo	atmo	nadir	albedo	atmo	B-norm	albedo
Blocks	0.95	0.87	0.79	0.79	15.0%	20.7%	21.5%
Vegetation	0.93	0.84	0.71	0.75	10.8%	12.2%	12.6%

## 9.2 BRDF-model variations: shape versus brightness

The scaling of albedo derived from the inversion of BRDF models relies on an adequate representation of the BRDF of individual pixels by the model derived from an image subset. To test the hypothesis of shape constancy, random samples of 200 pixels were taken from the used subsets and a BRDF model fitted. The result of 200 of such experiments were aggregated to provide an idea of the subset-internal variation in BRDF shape. The  $R^2$  describes the goodness of fit for the model. The means, standard deviations, minima and maxima for all 200 random experiments are calculated. The same statistics are provided for the shape of the model, defined by the ratio of the weights in the two kernel model. The total model brightness is given by the sum of both kernel weights. To relate the error in shape to an error in the inversion result, the white-sky integral is calculated from the kernel model using weights that represent the whole range of encountered shapes, while preserving its brightness. This approximates the shape-related error in white-sky albedo. The above parameters are shown for each used band in Figure 5.

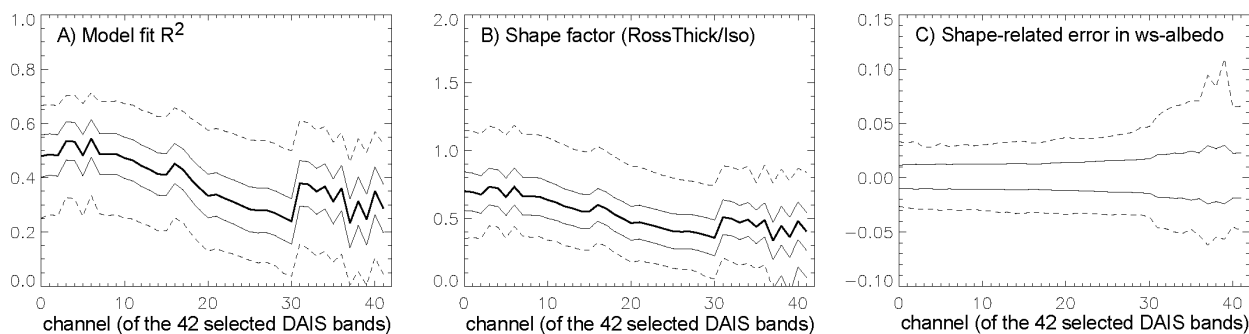


**Figure 5.** The variation of BRDF model shape within a subset of blocky surfaces in line 1 and its consequence on the derived white-sky albedo. Values are determined from 200 model inversion of 200 random samples each. Thick line: mean values; thin line: mean  $\pm$  1 Stdev; dotted line: min/max values. The shape-related error in white-sky albedo is given in absolute terms.

Table 5 provides an overview of the means over all bands for the parameters shown in Figure 5. Lines 1 and 2 were investigated using data taken from subsets representing blocky surfaces and alpine meadows. The error in white-sky albedo is given in relative terms.

**Table 5.** Indication of the variation of BRDF model shape within different subsets and its consequence on the derived white-sky albedo. Values are determined from 200 model inversion of 200 random samples each.

	No of Points	Model fit $R^2$	Standard deviation of $R^2$	Shape factor	Relative st. deviation of shape	White sky relative error
Line1_block	13821	0.384	$\pm 0.080$	0.534	23.6%	6.2%
Line2_block	20195	0.168	$\pm 0.088$	0.297	62.9%	11.7%
Line1_veg	54808	0.348	$\pm 0.074$	0.698	25.2%	7.4%
Line2_veg	35388	0.273	$\pm 0.085$	0.537	37.1%	9.4%

## 9.3 Comparison of modelled and measured broadband albedo

A BRDF model has been fitted for the rock glacier Murtèl independently for lines 1 and 2 based on a subset of 280 pixels as described in section 6. Inversion of this model was used to derive hourly albedo for a northern slope of  $10^\circ$  as described in section 7. This enables the comparison of a modeled and measured time series of albedo at the meteo station on Murtèl. For the snow-free period from 15 July to 15 September 1999, the measured albedo is 0.164; line 1 results in 0.197 and line 2 in 0.230. The differences in mean albedo are +0.03 (+20.2%) for line1 and +0.07 (+40.7%) for line 2. The difference between lines is 15.7%. The calculated albedo was not scaled to the meteo station pixel to avoid the influence of noise. The subset used for the model generation has a standard deviation of  $\pm 7\%$  in the image corrected albedo. Despite this offset between modelled and observed albedo, the temporal evolution of albedo is represented well (Figure 6).

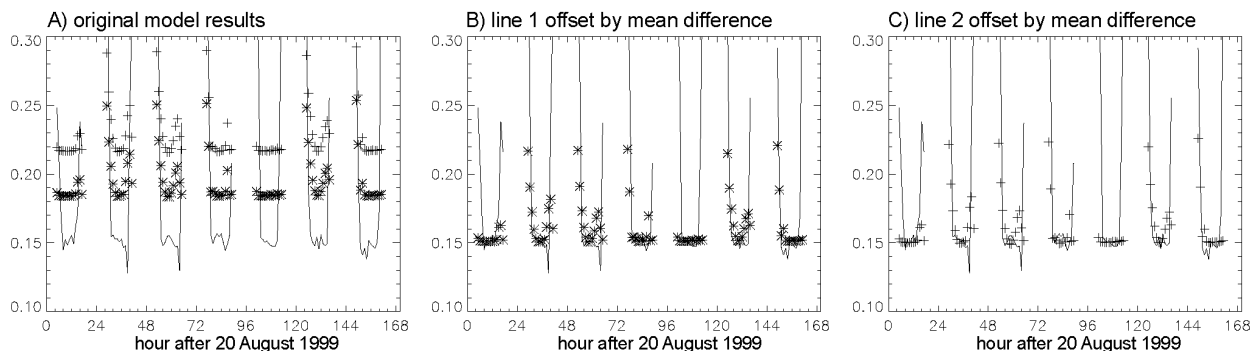


**Figure 6.** Comparison of measured broad-band albedo (line) with BRDF-model derived albedo for line 1 (x) and line 2 (+). A) absolute values; B+C) simulated values offset by mean difference to illustrate successful modeling of temporal albedo changes.

## 10 DISCUSSION OF ERRORS

In section 9 large differences between the means of subsets of lines 1 and 2 were shown. These differences are not lessened but amplified in the process of atmospheric and BRDF correction. It is assumed, that at least in part this is a problem of sensor stability.

In Section 7, it has been demonstrated, that the approximation of albedo by a constant (e.g. white-sky albedo) can result in an underestimation of albedo by 15-25% for steep slopes. The shape-related error in white-sky albedo here is in the order of 6-12%. Therefore it appears feasible to fit and invert a BRDF model and subsequently scale it to each image pixel.

The relative difference between image means presented in section 9.1 can be used as an indication of the standard deviation in the final albedo product being 13-22%. This would indicate, that the accuracy requirements defined for use in the model PERMEBAL are just met.

The large offset between modelled and measured albedo shown in 9.3 is striking. Even more so, because the difference between albedo derived from line 2 and measured albedo is largest, despite the fact, that vicarious calibration has been performed on line 2. Part of this deviation may be explained by the errors for the pyranometers and by the extreme heterogeneity of Murtèl Rock glacier. Nevertheless, an albedo of 0.23 appears to be rather large and open questions about the reason for his offset remain.

## 11 CONCLUSION

To the knowledge of the authors, this campaign has been the first time to employ airborne imaging spectrometry over such complex terrain. The successful geometric correction has been demonstrated. The complex topography results in a much larger range and much larger variability of sun-target-sensor geometries. As a consequence, correction of the effects of atmospheric interaction, varying illumination and angular anisotropy is much more important than in gently sloping terrain, if the quantitative extraction of surface characteristics is desired. At the same time, this correction is greatly affected by noise in the digital elevation data that is used for correction. The fundamental problem of adequate representation of surfaces and the generation of its derivatives is amplified by errors introduced by inaccurate spatial co-registration.

It was demonstrated, that kernel-based BRDF models could successfully be fitted on subscenes and the information so gained applied for the derivation of albedo for each pixel.

Coupling of an image-derived BRDF model with the radiation module of the energy-balance program PERMEBAL revealed, that angular anisotropy has a significant influence on the ground surface energy balance.

## ACKNOWLEDGMENTS

This project has been carried-out in the Swiss National Foundation project "Analysis and spatial modeling of permafrost distribution in cold-mountain areas by integration of advanced remote sensing". Further support has been provided by the EU-program HySens. Dr. Andreas Kaeaeab kindly provided the digital elevation model used. Many thanks to Gabriela Schaeapman-Strub and especially Dr. Stefan Dangel for their help and discussions on the

treatment of angular anisotropy. The authors also wish to thank Dr Rolf Richter and Stefanie Holzwarth of the German Aerospace Center (DLR) for their cooperation and help throughout this study.

## REFERENCES

- [1] STOCKER-MITTAZ, C., HOELZLE, M., AND HAEBERLI, W. 2002: Modelling Alpine permafrost distribution based on energy-balance data: a first step. *Permafrost and Periglacial Processes* 13, pp 271-282.
- [2] MITTAZ, C., HOELZLE, M., AND HAEBERLI, W. 2000: First results and interpretation of energy flux measurements of Alpine permafrost. *Annals of Glaciology* 31, pp 275-280.
- [3] WANNER, H., GYALISTRAS, D., LUTERBACHER, J., RICKLI, R., SALVISBERG, E. & SCHMUTZ, C. 2000: Klimawandel im Schweizer Alpenraum. *Final Report of the Swiss National Research Program 31*, vdf, Hochschulverlag AG, ETH Zürich, 296 pp.
- [4] OHMURA, A., BENISTON, M., ROTACH, M., TSCHUCK, P., WILD, M. AND MARINUCCI, M. 1996: Simulation of Climate Trends over the Alpine Region. *Final Report of the Swiss National Research Program 31*, vdf, Hochschulverlag AG, ETH Zürich, 285 pp
- [5] HAEBERLI, W., KÄÄB, A., HOELZLE, M., BÖSCH, H., FUNK, M., VONDER MÜHLL, D. AND KELLER, F. 1999: Eisschwund und Naturkatastrophen im Hochgebirge. *Final Report of the Swiss National Research Program 31*, vdf Hochschulverlag an der ETH Zürich. 190 pp.
- [6] MITTAZ, C., IMHOF, M., HOELZLE, M., AND HAEBERLI, W. 2002: Snowmelt evolution mapping using an energy balance approach over alpine terrain. *Arctic, Antarctic and Alpine Research* 34(3), pp 274-281.
- [7] NICODEMUS, F.E., RICHMOND, J.C., HSIA, J.J., GINSBERG, I.W. AND LIMPERIS, T. 1977: Geometrical Considerations and Nomenclature for Reflectance, U.S. Department of Commerce, National Bureau of Standards.
- [8] MARTONCHIK, J.V., BRUEGGE, C.J. AND STRAHLER, A.H. 2000: A review of reflectance nomenclature used in remote sensing. *Remote Sensing Reviews*, Vol. 19, pp. 9-20.
- [9] BEISL U. 2001: Correction of Bidirectional Effects in Imaging Spectrometer Data. PhD Thesis, *Remote Sensing Series* 37, RSL, University of Zurich, pp. 189.
- [10] LUCHT, W., C.B. SCHAAF, AND A.H. STRAHLER. 2000: An Algorithm for the retrieval of albedo from space using semiempirical BRDF models. *IEEE Trans. Geosci. Remote Sens.*, 38, 977-998.
- [11] ROUJEAN, J-L., M. LEROY, AND P-Y. DESHAMPS. 1992: A bidirectional reflectance model of the earth's surface for the correction of remote sensing data. *J. Geophys. Res.*, 97(D18), pp 20455-20468.
- [12] WANNER, W., LI, X., & STRAHLER, A. 1995: On the derivation of kernels for kernel-driven models of bidirectional reflectance. *J. Geophys. Res.*, 100(D10), pp 21077-21089.
- [13] HOELZLE, M., VONDER MÜHLL, D. AND HAEBERLI, W. 2002: Thirty years of permafrost research in the Corvatsch-Furtschellas area, Eastern Swiss Alps: a review. *Norwegian Journal of Geography*. 56(2), 137-145.
- [14] STROBL, P., NIELSEN, A., LEHMANN, F., RICHTER, R. AND MUELLER, A. 1996: DAIS System Performance, First results from the 1995 Evaluation Campaigns. *Proc. 2nd International Airborne Remote Sensing Conference and Exhibition, San Francisco*, Vol. II, pp. 325-334.
- [15] SCHLÄPFER, D. AND RICHTER, R. 2002: Geo-atmospheric Processing of Airborne Imaging Spectrometry Data Part 1: Parametric Orthorectification. *International Journal of Remote Sensing*, 23, pp. 2609-2630.
- [16] RICHTER R. AND SCHLÄPFER D. 2002: Geo-atmospheric Processing of Airborne Imaging Spectrometry Data Part 2: atmospheric/topographic correction. *International Journal of Remote Sensing*, 23, pp. 2631-2649.
- [17] BERK, A., BERNSTEIN, L.S., ANDERSON, G.P., ACHARYA, P.K., ROBERTSON, D.C., CHETWYND, J.H. AND ADLER-GOLDEN S.M. 1998: MODTRAN Cloud and Multiple Scattering Upgrades with Application to AVIRIS. *Remote Sens. Environ.* 65, pp. 367-375.
- [18] COLLAR-PEREIRA, M. AND RABL, A. 1979. The average distribution of solar radiation correlations between diffuse and hemispherical and between daily and hourly insolation values. *Solar Energy* 22, pp 155-164.